Tactile-Sensitive Artificial Skin for Multiaxial Force Detection and Texture Recognition

Chern Yang Leong, Jingxian Cui, Xin Cheng, Lin Htein, and Hwa-Yaw Tam, *Life Fellow, IEEE, Fellow, Optica*

***Abstract*—Tactile perception, particularly at the fingertips, is fundamental to human dexterity, enabling fine motor control and reliable manipulation of objects through the precise real-time modulation of normal and shear forces based on encountered frictional conditions. To bridge this capability gap in robotics, a novel tactile-sensitive artificial skin is designed to significantly enhance robot-object interaction and environmental recognition. The artificial skin, fabricated from a 2-mm thick silicone elastomer membrane embedded with polymer optical fiber Bragg grating (FBG) sensor array, achieves large measurement range (detecting forces up to 10 N normal and ±4 N shear) and high sensitivity for multiaxial forces. The skin's performance was evaluated through tests involving normal force loading of up to 10 N and shear force loading around ±4 N using a three-axis translation gantry. Additionally, the study examines slip-induced vibrations on various textured surfaces. A multi-input multi-output convolutional neural network (MIMO-CNN) was developed to simultaneously estimate force and recognize textures based on multichannel FBG inputs. The MIMO-CNN achieved an R-squared value of 0.96 for force estimation and classification accuracy of 94 % for texture recognition across 20 fabric samples. These findings highlight the potential of tactile-sensitive artificial skin to enhance robotic perception and manipulation, paving the way for more advanced humanoid robotic systems.**

***Index Terms*—Artificial skin, fiber Bragg gratings, multiaxial force detection, polymer optical fiber, robotic tactile perception, texture recognition.**

I. Introduction

THE growing demand for humanoid robots capable of seamlessly integrating into human environment and performing a wide range of tasks has recently sparked increasing research interests and market demands [1], [2], [3]. In many scenarios, humanoid robots are expected to replicate human-like activities in unstructured settings, either to assist humans in a shared space or to operate in an unsafe environment for humans. These situations usually involve interacting with tools and equipment designed for human ergonomics which heavily rely on tactile perception [4], [5], [6].

Tactile perception, especially at the fingertips, is essential for fine motor control and dexterous object manipulation, enabling reliable interaction with surrounding objects. At the initial point of contact in most interactions, it is important for robotic fingers to have sensory feedback, especially normal and shear force, with high tactile sensitivity and spatial acuity [7]. Dexterous manipulation requires balancing normal and shear forces between the finger and the object for effective interaction [8]. During human-object interaction, these forces are controlled in real time based on different frictional conditions [9]. For instance, grips are tightened for slippery objects to prevent slipping and loosened for rough, sticky objects. In some cases, slip is intentionally introduced by gently sliding the fingertip across the object's surface to acquire texture information [4]. This multidimensional tactile information, along with other sensory feedback, can be further analyzed to recognize complex features of the object, ultimately enabling robots to mimic human in object recognition [4] and strategize for effective manipulation.

While multiaxial force sensors are used in robotic joints for load and grip monitoring as well as tactile sensing, they are usually fabricated on rigid substrates [10] and are not optimized for curved and complex surfaces, making them unsuitable for replicating tactile perception in robots especially at the fingertip. On the other hand, the emergence of soft sensing devices has led to the development of tactile-sensitive artificial skin, a sensor-rich synthetic material designed to mimic the properties and tactile sensing capabilities of human skin. Various implementations of tactile-sensitive artificial skin on robots and prosthetics utilize various sensing mechanisms such as resistive [11], [12], [13] and capacitive [14], [15], [16] sensors. However, electronic sensors are generally susceptible to electromagnetic interference from the surrounding environment or near power lines within the robot, limiting their use in harsh environments [17]. Furthermore, electronic sensors require large number of electrical connections as the number of sensing elements increase, limiting their functionality in large area and high-spatial-resolution tactile sensing where many tactile sensors are distributed across a robotic surface.

Fiber Bragg gratings (FBGs) are excellent sensing elements for tactile-sensitive artificial skin due to their

This work was supported in part by Department of Science and Technology of Guangdong Province under Project K-ZGAR, The Hong Kong Polytechnic University (UGC) 1-CDJ0, and Hong Kong Baptist University H-ZL26. *(Corresponding author: Jingxian Cui).*

Chern Yang Leong, Jingxian Cui, Lin Htein, and Hwa-Yaw Tam are with Photonics Research Institute, Department of Electrical and Electronic Engineering, The Hong Kong Polytechnic University, Hong Kong SAR (e-mail: chern-yang.leong@connect.polyu.hk, jing-xian.cui@polyu.edu.hk, htein.lin@polyu.edu.hk, hwa-yaw.tam@polyu.edu.hk).

Xin Cheng is with Department of Electrical and Electronic Engineering, The Hong Kong Polytechnic University, Hong Kong SAR (e-mail: xin.cheng@polyu.edu.hk).

small form factor, fast response time and excellent multiplexing capability, enabling multiple FBGs to be incorporated serially in a single optical fiber while retaining the advantages of optical fiber such as immunity to electromagnetic interference and resilience in harsh environment. Furthermore, the properties of each FBG within the optical fiber such as grating length, central wavelength and location along the fiber can be customized to optimize detection of different tactile stimuli at different locations on the robot. FBG-embedded artificial skin has been previously demonstrated on robotic arms [18] and fingers [19], featuring its tactile sensing capabilities and skin-like form factor. To fully exploit the multiplexing capability of FBGs, all FBGs should ideally be cascaded along a single optical fiber strategically routed throughout the sensing area. Each FBG is spaced apart to create a quasi-distributed sensing configuration. Conventional FBGs are mostly based on silica optical fiber which, due to its brittle nature, are prone to breakage when bent excessively. When optical fibers are routed across small areas, tight bends are usually necessary, limiting their application to larger surfaces.

Polymer optical fibers (POFs) on the other hand, could potentially replace silica optical fibers for distributed tactile sensing in small areas [20]. Due to their lower Young's modulus, POFs are more resilient to bending compared to silica optical fibers of similar diameter, allowing tight bending without the risk of breakage [21]. This enables robust placement of polymer optical fiber Bragg gratings (POFBGs) on both small and large areas without compromising the advantages offered by silica-based FBGs [22], [23]. Furthermore, their lower Young's modulus enhances the strain sensitivity of POFBGs [22], expanding their force-sensitive area when embedded into an elastic material for artificial skin applications. The expanded force sensitive region reduces the number of FBGs required for coverage over a specific area, decreasing the computational requirements for large area tactile sensing.

In this work, we introduce a tactile-sensitive artificial skin made of silicone and embedded with a three-element FBG array inscribed along a single-mode POF made of cyclo-olefin polymer (ZEONEX™), which has very low water-affinity. The artificial skin mimics the dimensions of human skin and features a fingerprint-like pattern with a triangular profiled spiral to facilitate vibration generation during slip. A multi-input multi-output convolutional neural network (MIMO-CNN) is developed to simultaneously estimate normal and shear forces based on FBG responses while recognizing textures based on vibrational responses, replicating human-like tactile perception and texture recognition capabilities. The proposed system achieved a strong correlation for force estimation and high accuracy for texture classification, with values of 0.96 and 94% respectively, establishing a robust framework for tactile sensing in humanoid robots. The implications of this work extend to improving human-robot interaction in applications ranging from assistive technology to automated industrial tasks.

II. Design and Fabrication

The artificial skin consists of three cascading FBGs inscribed along an in-house fabricated single-mode step-index ZEONEX POF using the "pull-through" method [24], [25], with a core diameter of 8 µm and outer diameter of 160 µm. The ZEONEX POFBGs are embedded within a 2-mm thick silicone elastomer layer, similar to the thickness of human skin [26], which was molded on a base with dimensions comparable to the human index finger. The artificial skin replicates the depth-wise hardness gradient of the human skin using a bilayer silicone structure, where a soft base layer (Shore-A 0) mimics the dermis and a stiffer encapsulating layer (Shore-A 40) replicates the epidermis [26]. Despite not replicating the exact stiffness of the human skin (Shore-A 13–28) [27], [28], [29], this biomimetic stiffness distribution, where the top layer is harder than the base, facilitates slip-induced vibration detection. Before sensor fabrication, thermal annealing was performed at 90 °C for 24 hours to remove residual stress [30] induced during the fiber drawing process. Each FBG was fabricated using the phase mask technique with a single 248-nm KrF excimer laser pulse. The reflection spectrum of the embedded FBG array is shown in Fig. 1(b) and all four FBGs are each 2 mm long and spaced 12.5 mm apart (center-to-center), as illustrated in Fig. 1(c).

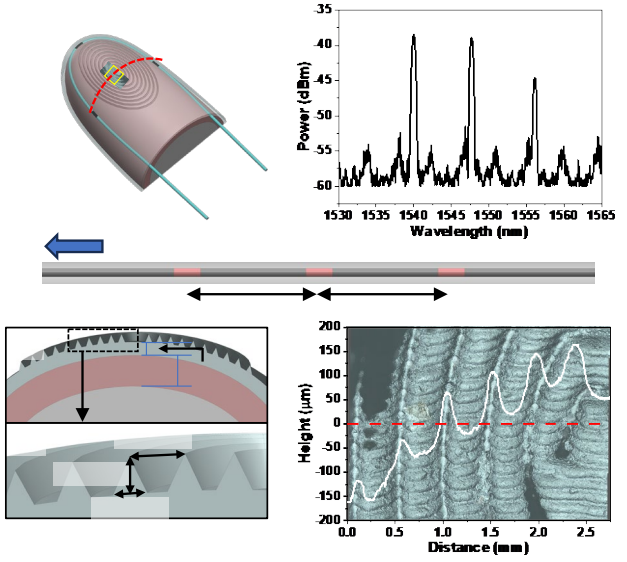

Fig. 1. (a) Illustration of the fingertip phantom covered with tactile-sensitive artificial skin. (b) Reflection spectra of the FBG array embedded within artificial skin. (c) Dimensions and location of the FBG array along ZEONEX POF. (d) Cross-sectional view of the artificial skin along the dotted line in (a). (e) Enlarged view of the triangular profile resembling fingerprint ridges. (f) Laser confocal micrograph of the area highlighted by the yellow box in (a) along with the measured line profile of the fingerprint ridges along dotted line in (a).

The POF is routed so that FBG1 and FBG3 run parallel to the finger, while FBG2 is perpendicular to them, allowing for effective monitoring of deformations in the artificial skin by multidirectional forces. Prior to molding, the POF inscribed with FBGs was treated with a silicone primer (Dowsil™ 1200 OS) to improve silicone adhesion, and a two-step molding process [20] was used, with triangular-profiled spirals incorporated onto the 3D-printed mold surface with printing resolution of 20 µm. As smaller fingerprint ridges allow smaller distinguishable feature [4], a triangular profile is selected to minimize the tip size and a spiral pattern is employed to introduce varied pitch distances to ensure versatility for different textures. The base width, ridge height and ridge-to ridge distance of the fingerprint are approximately 0.3 mm, 0.4 mm and 0.5 mm respectively, closely resembling the dimensions of human fingerprint ridges [31] while taking into account the printing resolution of the molds. The dimensions of the artificial skin and the fingerprint are shown in Fig. 1(d) and Fig. 1(e), respectively. The laser confocal micrograph highlighting the surface profile of the artificial skin is shown in Fig. 1(f) and the overlaid plot represents the line profile of the surface along the dotted line. The line profile is measured orthogonally with respect to the fingerprint ridges, indicating the dimensions of the molded fingerprint ridges. Generally, the fingerprint ridges are rounded on the tip due to limitation in 3D-printing resolution and the resulting tip diameter was found to be around 80 µm.

III. Characterization of Tactile-Sensitive Artificial Skin

The experimental setup for applying multidirectional force is shown in Fig. 2(a). It consists of a 3-axis electronic platform with three precision stages mounted orthogonally to each other. An L-shaped aluminum attachment is secured to the translation platform, creating a levelled flat contact surface that faces the fingertip for applying normal and lateral forces through the movement of the contact surface.

The platform's contact surface is polished to minimize wear on the artificial skin during lateral force application. Beneath the levelled platform, the fingertip phantom with integrated tactile-sensitive artificial skin is attached to a three-axis load cell (Simbatouch), which captures the forces acting on the fingertip phantom. The load cell has a detection range of 10 N for Z-axis and ±5 N for X and Y-axis with resolution of 0.1 N. The reflection spectrum is acquired by an FBG interrogator (Luna, HYPERION si255) and the Bragg wavelength of each FBG is recorded at a rate of 5 kHz. The movements of the 3-axis platform, the load cell response, and the response of each FBG are controlled and recorded simultaneously through an integrated LabVIEW interface. Fig. 2(b) illustrates movements of contact surface to apply force to the fingertip surface. Generally, applying normal force involves vertical translations of the contact surface, as depicted in Fig. 2(b-ii) and Fig. 2(b-vi), while shear force application involves lateral translation of the contact surface relative to the fingertip.

A. Multidirectional Force Characterization

As illustrated in Fig. 2(b), the application of normal force on the artificial skin involves a Loading phase, followed by Unloading phase. During the Loading phase, the contact platform is lowered at a speed of 0.5 mm/s until a normal force of 10 N is exerted, which is approximately the typical human grip force [32] . Then the platform's position is then held for 5 seconds before the Unloading phase, where the platform is retracted upwards at the same speed of 0.5 mm/s.

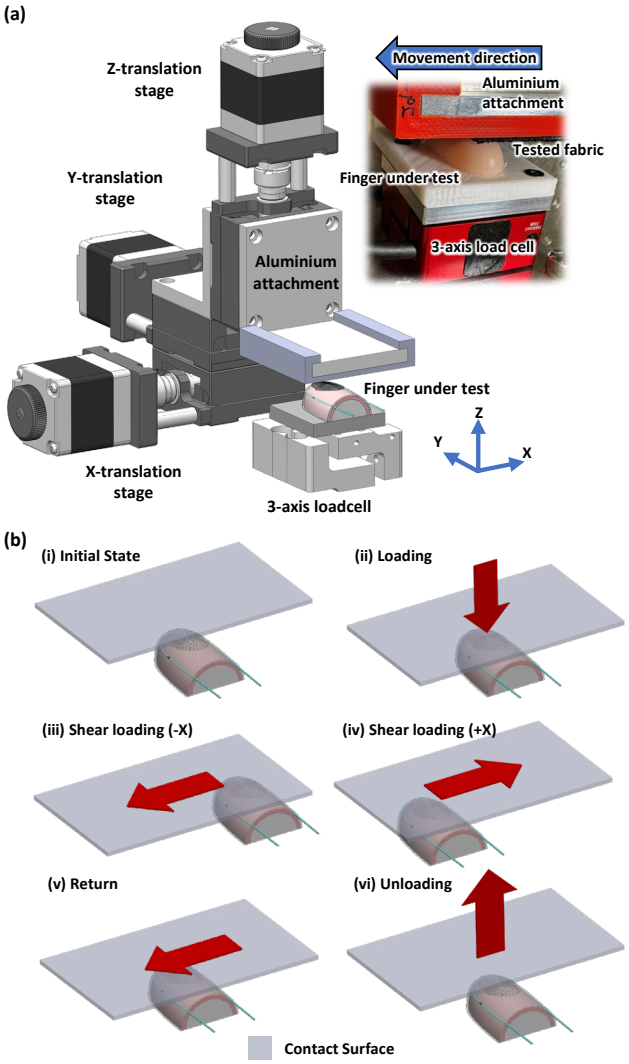

Fig. 2. (a) Diagram of the experimental setup for characterizing the artificial skin (inset: photograph of fingertip under fabric sliding test condition) and (b) the movement of the contact surface for applying normal and shear force on the fingertip: (i) Initial state: the surface is not in contact with fingertip, and no force is applied; (ii) Loading: the surface is lowered until specified normal force is applied to the fingertip; (iii-iv) Shear loading: the contact surface is moved laterally (shown in the ±X direction) to apply shear force; (v) Unloading: the contact surface is lifted from the fingertip, releasing all forces.

To evaluate the shear force response, the sequence of motions is Loading, Shear loading the negative direction,

Shear loading the positive direction, and then Unloading. Initially, the contact platform is lowered to apply normal force, allowing shear to be transferred to the artificial skin through friction between the contact surface and the skin. The platform is then moved laterally to apply shear force until slipping occurs between the artificial skin and the contact surface. The lateral movement is then reversed to apply shear force in the opposite direction until slipping occurs again, after which the platform returns to the center, and the contact surface is retracted. These movements are performed on both the ±X and ±Y directions.

B. Slip-Induced Vibration Acquisition

When the applied shear force exceeds the static friction between the finger and the contact surface, slip occurs, generating vibrations whose characteristics depend on factors such as surface texture. To capture slip-induced vibrations between the fingertip and various textured surfaces, twenty different fabric samples were prepared, as shown in the photographs in Fig. 3(a). The surface roughness of all fabric samples was measured using a laser confocal microscope and their respective arithmetic surface roughness (Ra) and average maximum height (Rz) values are plotted in Fig. 3(b), where larger values indicate higher surface roughness.

The fabric samples consist of a variety of roughness, with Ra values ranging from 7.8 µm to 121.6 µm and Rz values ranging from 87.4 µm to 1234.4 µm. It is also worth mentioning that several fabric samples, particularly sample 11, 12, 17, 18 and 19 have similar roughness values, which maybe be difficult to differentiate if recognition is solely based on surface roughness. Such fabric collection allows thorough investigation of texture recognition performance of the artificial skin. Each fabric sample was attached to the contact surface and lowered onto the fingertip to apply a specified initial normal force. The surface was then laterally translated by 50 mm in both the ±X and ±Y directions, one after another, to induce slip while maintaining the fingertip's vertical position. The 50 mm lateral translation distance is sufficient to apply shear force beyond the sliding threshold of all fabric samples and the fingertip surface. The sliding tests were repeated with varying initial normal forces and sliding speeds for all 20 fabric samples, as detailed in Table 1, while the wavelength shifts of each FBG were recorded at a rate of 5 kHz.

IV. Characteristics of Tactile Sensitive Artificial Skin

A. Multidirectional Force Sensitivity

Fig. 4 depicts the force response of all embedded FBGs to normal and shear forces along the X- and Y-directions. As shown in Fig. 4(a), each FBG exhibits a linear response to normal force up to 10 N, with sensitivities of 219.0 pm/N, 381.4 pm/N and 283.5 pm/N for FBG1, FBG2 and FBG3,

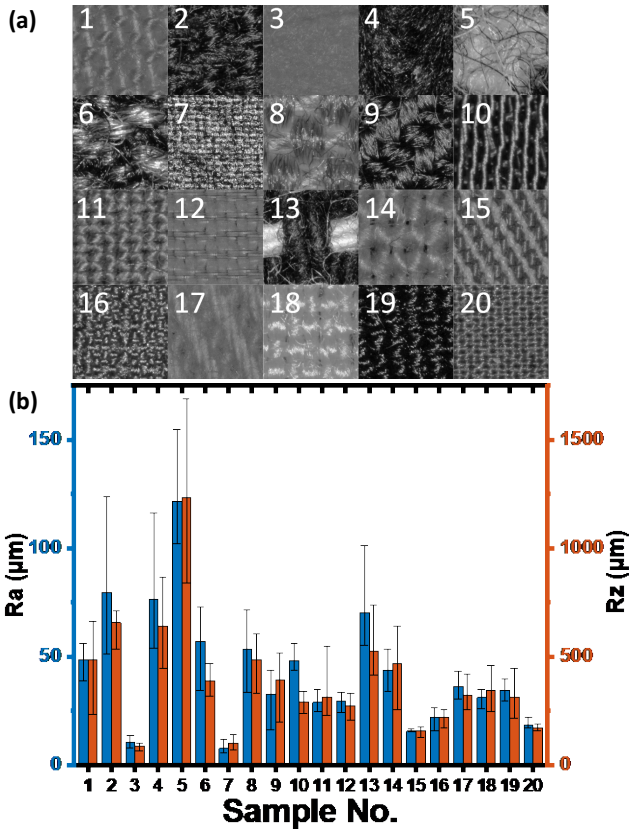

Fig. 3. (a) Photographs of the 20 fabric samples, each labelled with number on the top left corner. Field of view: 2 mm × 2 mm. (b) Arithmetic average roughness (Ra) and average maximum height (Rz) of the fabric samples, averaged across 10 measurements.

TABLE I
IMPLEMENTED INITIAL CONDITIONS OF SLIDING TESTS

Test no.	Initial normal force (N)	Sliding speed (mm/s)	Sliding distance (mm)
1	1	2	50
2	1	4	50
3	2	2	50
4	2	4	50

respectively. The variation in sensitivities is mainly due to difference in position and the distance between the load center and each FBG element. This configuration of FBG embedded in an elastomer creates a force receptive region with maximum sensitivity at the center of the FBG, which gradually decreases as the distance between the applied normal force and the FBG increases [20]. Due to the viscoelastic nature of the silicone elastomer, all three FBGs exhibit hysteresis error, quantified as 10.3%, 10% and 11% for FBG1, FBG2, and FBG3, respectively, using Eq. (1) [33]. The hysteresis, $H(\%fs)$, expressed as a percentage of maximum wavelength shift, is defined by the ratio between the maximum uncertainty of wavelength shift during loading and unloading at a given applied force, and the full-

scale wavelength shift when a maximum force of 10 N is applied.

$$H(\%fs) = \frac{\max(\Delta\lambda_{unload} - \Delta\lambda_{load})}{\Delta\lambda_{max}} \times 100\% \qquad (1)$$

The shear force response along X- and Y-directions of the embedded FBG array are depicted in Fig. 4(b) and Fig. 4(c), respectively. To apply shear force to the fingertip surface, an initial normal force of 6 N was applied before introducing shear forces. The shear force measurement range of the multiaxial load cell was limited to ± 5 N, and contact force of 6 N was selected such that slipping occurs just below 5 N at one of the four shear directions During the application of shear force, the experiment setup was adjusted so that shear force was applied in only one direction when the aluminum contact surface was moved in the desired direction, with forces on all three axes being monitored and recorded. This adjustment ensured that the FBG response due to normal force during shear force application is effectively cancelled out, making the shear force in the orthogonal direction negligible.

The shear force response in the X-direction is depicted in Fig. 4(b). It can be observed that FBG1 and FBG3 exhibit a linear response to X-direction shear force with low hysteresis errors of 4.59% and 3.38%, respectively. Linear fitting on FBG1 and FBG3 yield sensitivities of 659.4 pm/N and −881.9 pm/N, respectively. However, while FBG2 shows a linear response, its response deviates from linearity when shear forces exceed 3 N in the X-direction, with relatively larger hysteresis error of 14.81%. Similarly, for Y-direction shear, as shown in Fig. 4(c), FBG1 and FBG3 exhibit larger hysteresis compared to FBG2, which shows a linear response to shear force applied in the Y-direction with a sensitivity of −396.8 pm/N. The hysteresis errors were found to be 28.45%, 5.69%, and 39.57% for FBG1, FBG2, and FBG3, respectively. Overall, the embedded FBGs demonstrate optimal performance, characterized by strong linearity and minimal hysteresis error, when shear forces are applied perpendicular to their orientation. The use of a soft skin layer (Shore-A 0) facilitates enhanced sensitivity, despite causing relatively high hysteresis error [34] when shear aligns parallel to the FBGs. For effective measurement of shear in both X- and Y-directions, the embedded POF routes FBG2 orthogonally to FBG1 and FBG3.

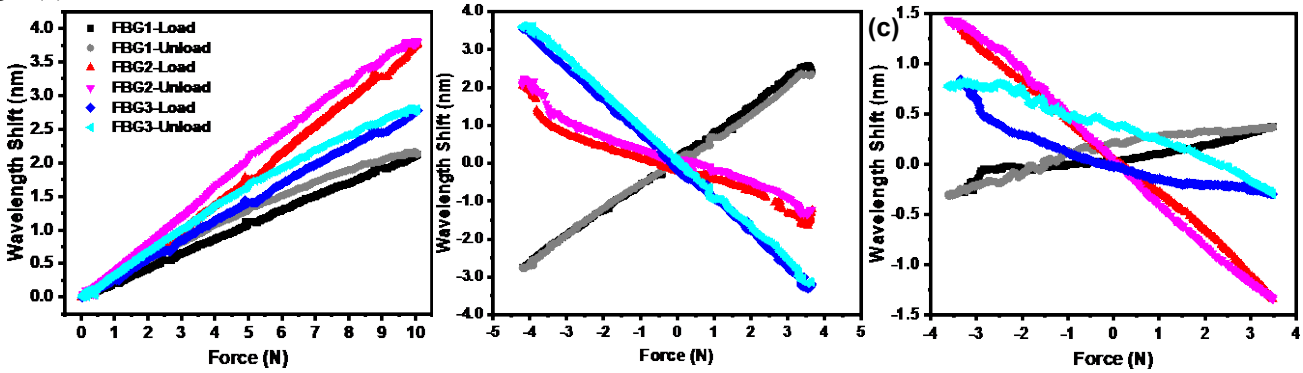

Fig. 4. Response of embedded POFBG array to (a) normal force, (b) shear force along the X-axis, and (c) shear force along the Y-axis.

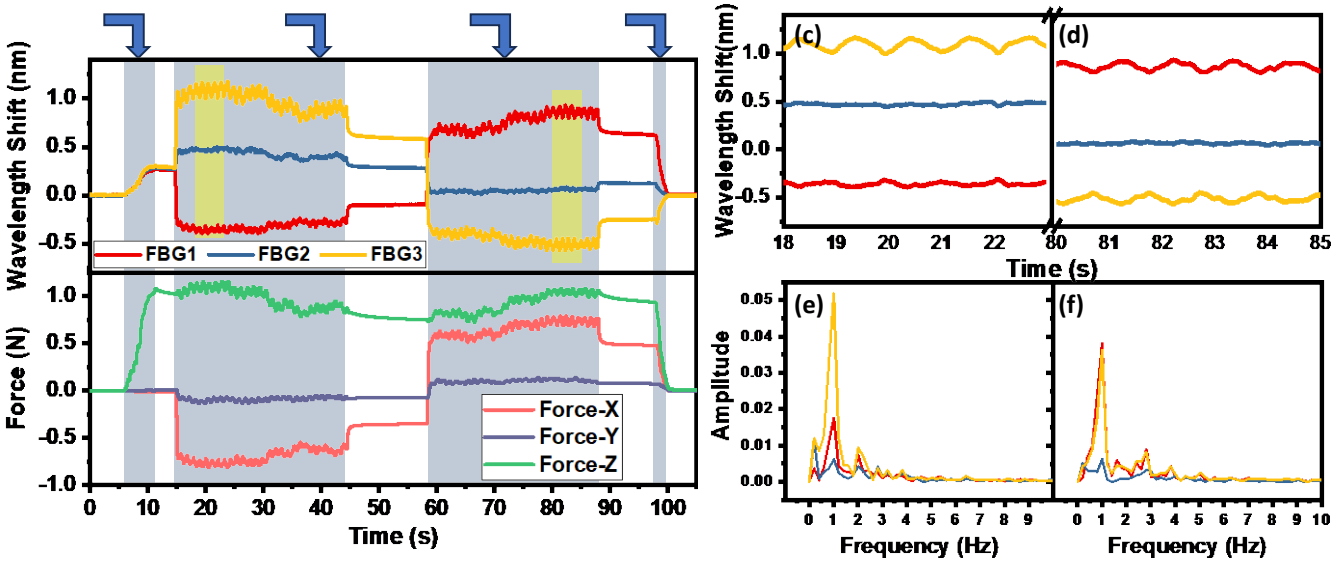

Fig. 5. (a) Recorded wavelength response of FBG array. (b) Multiaxial force experienced by the fingertip during slipping between the artificial skin and fabric sample 17 along the ±X axis at 2 mm/s. Transient response during slip in the (c) −X and (d) +X direction. FFT spectra of the FBG response during slip in the (e) −X and (f) +X direction, with time windows sampled from the regions highlighted in yellow in (a).

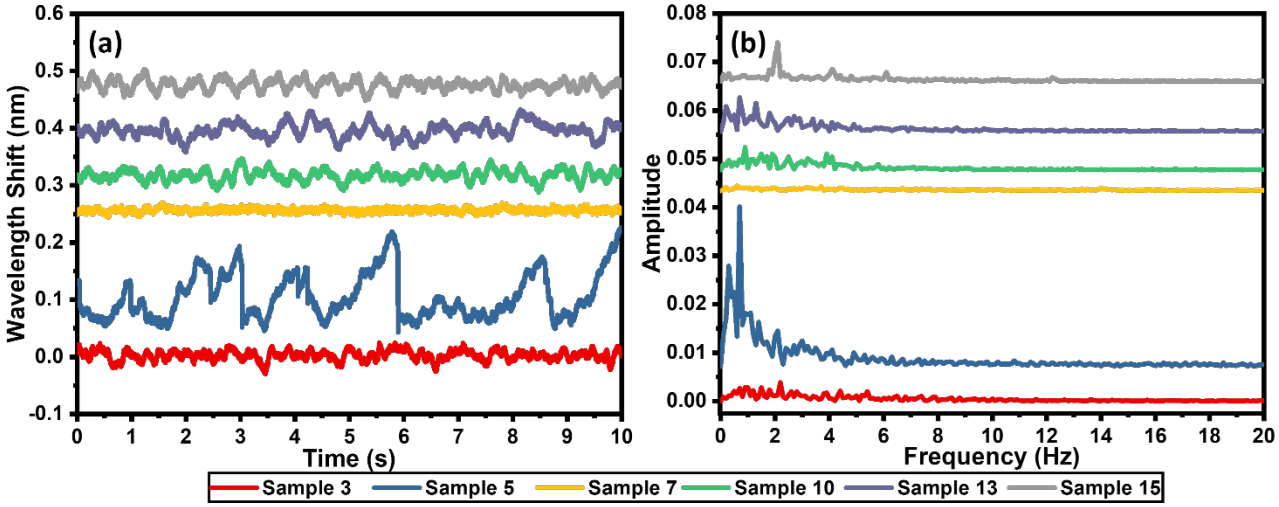

Fig. 6. (a) Vibration signals acquired by FBG1 from selected fabric samples at a sliding speed of 2 mm/s and (b) their respective FFT spectra.

B. Slip-Induced Vibration Characteristics

Fig. 5(a) shows the transient response of FBG array, while Fig. 5(b) illustrates the corresponding forces exerted on the fingertip when fabric sample 17 slides across the fingertip surface at a speed of 2 mm/s. As seen in Fig. 5(a) and Fig. 5(b), the forces experienced by the artificial skin are reflected in the FBG response. During the loading phase, all FBGs experience redshift when a normal force of 1 N is applied to the artificial skin. At t = 15 s, shear loading is applied, indicated by an increase in the −X direction force. Each FBG responds differently to the applied shear force due to its distinct positions and orientations across the artificial skin. Initially, as fabric sample 17 slides across the artificial skin, the applied shear force rapidly spiked and saturated around −0.7 N as the fabric slips, generating vibrations. This is indicated by the oscillations in the FBG response and the recorded force values. At t = 60 s, when fabric sample 17 is slid in the +X-direction, a similar response with the shear force saturating around 0.7 N and vibration occurring as slipping continues.

Fig. 5(c) and Fig. 5(d) display 5-second windows of the FBG vibrations during slipping in the −X and +X directions and their fast Fourier transform (FFT) spectra is as shown in Fig. 5(e) and Fig. 5(f), respectively. These results reveal sliding fabric sample 17 in both directions at 2 mm/s results in similar frequency components, with a prominent frequency of 1.00 Hz. It is noted that FBG1 and FBG3 are more sensitive to slip along X direction compared to FBG2, as indicated by the vibration amplitude and the and peak intensity in their respective FFT spectra.

Fig. 6(a) shows the vibration response of FBG1 when the artificial skin slides across fabric samples 3, 5, 7, 10, 13 and 15 at a speed of 2 mm/s towards +X direction, with their respective FFT spectra shown in Fig. 6(b). Under the same conditions, the vibration amplitude and frequency generated by each fabric sample differ. Generally, rougher fabrics produce vibrations with larger amplitudes and lower frequencies, and vice versa. For instance, fabric sample 5, the roughest of all 20 samples as indicated by its Ra and Rz values, exhibits a vibration signal with a peak-to-peak amplitude of approximately 0.25 nm and a prominent frequency of 0.7 Hz. In contrast, the vibration generated by sliding across fabric sample 10 exhibit a peak-to-peak amplitude of about 0.06 nm and a prominent frequency of 0.9 Hz as it is smoother than fabric sample 5. Fabric sample 7, the smoothest among all samples, generates virtually no vibration.

C. Long-Term Stability

The long-term stability of the artificial skin was investigated. Fig. 7 depicts the cyclic pressure response, where rapid loading and unloading of normal force was applied on the artificial skin over 10000 cycles between 1 and 3 N at 1-second interval. Throughout the 10000 force cycles, no significant drift nor signal degradation was observed, and the signal maintained a repeatable and stable wavelength response, indicating long-term stability and durability.

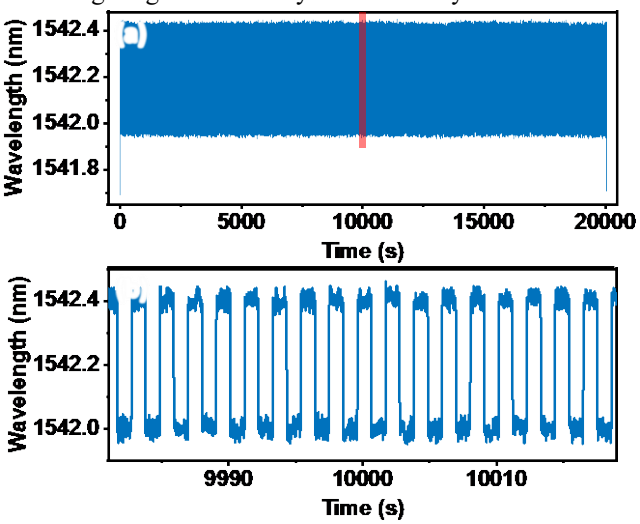

Fig. 7. (a) Cyclic wavelength response of FBG1 towards 10000 rapid normal force loading cycles between 1 and 3 N at 1-second interval. (b) Zoom-in view of wavelength response from 9980 to 10020 second (highlighted red in (a)).

V. Force Estimation and Texture Recognition

Different surfaces interact differently with the artificial skin, producing distinct vibrations during slipping that are unique to each slipping surface. With an algorithm capable of analyzing these vibrational responses, different textures can be recognized and differentiated. While it is possible to numerically estimate the forces applied to the artificial skin, this approach is less practical for tactile-sensitive artificial skin designed for humanoid robots due to the complex curvatures and shapes involved, which led to cumbersome calculations. Additionally, precise knowledge of the position and orientation of the FBGs is required, imposing strict tolerance necessitating tedious calibration procedure [20]. Furthermore, tactile exploration, especially in open environment, involves multidimensional stimuli such as pressure, vibration, temperature and pain which are deeply intertwined [35], [36]. Distinguishing these stimuli requires a robust algorithm capable of processing large and complex datasets while learning and adapting to new data in real-time.

Neural networks, especially convolution neural networks (CNNs) [37], [38] are well-suited for decoding tactile stimulus due to their excellent performance in handling large volume, nonlinear and multidimensional data. Being data-driven, CNNs can inherently compensate for fabrication errors and tolerances in the artificial skin. Additionally, CNNs offer inherent robustness to noise and input variations [37]. This allows raw and multidimensional tactile signals which in our case, consists of intercoupled forces and vibrations signals, to be input directly with minimal preprocessing. The CNN internally decouples and extracts individual component from the multichannel sensor signals. They also support transfer learning, allowing pre-trained model parameters to be fine-tuned for new events and stimuli, mimicking human learning by correlating past experiences with new situations.

In this study, a MIMO-CNN was developed using the Keras library to simultaneously estimate the normal and shear forces experienced by the fingertip and classify the contact surface

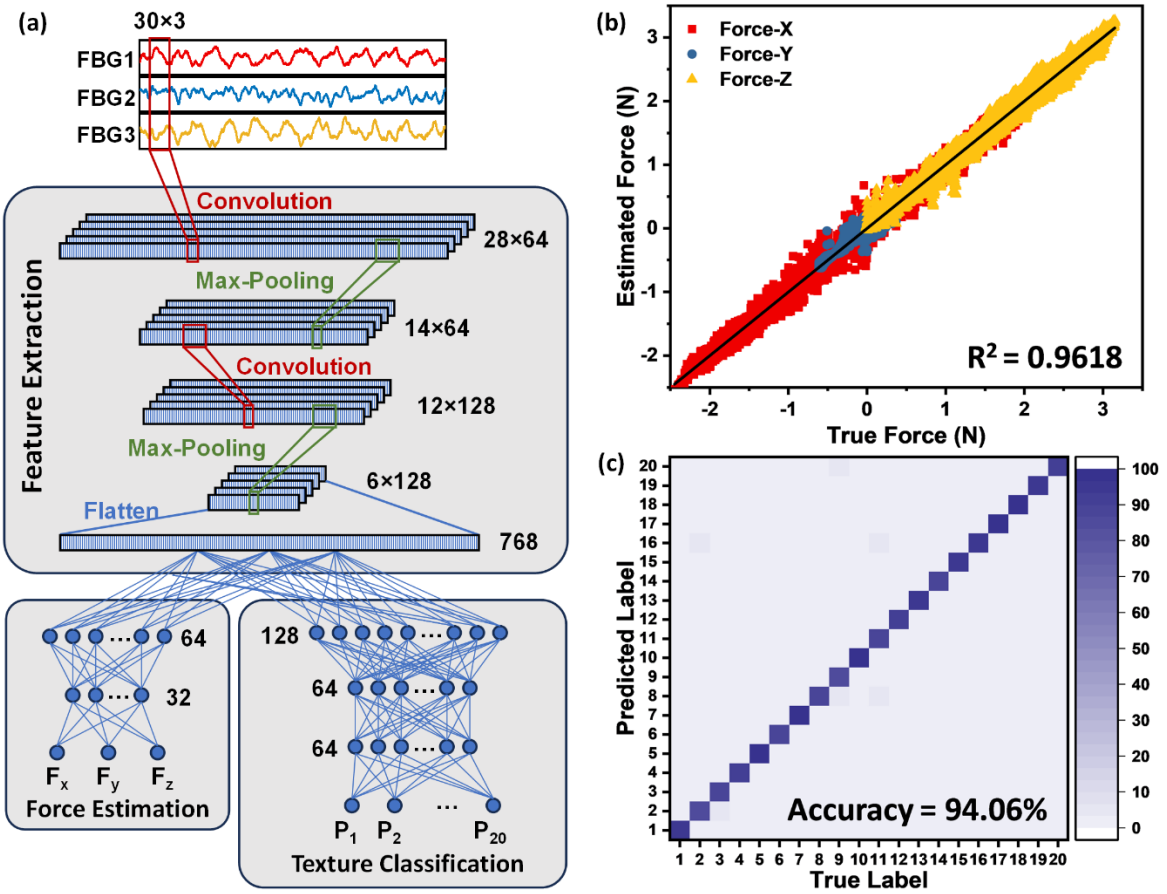

Fig. 8. (a) Illustration of MIMO-CNN architecture. CNN output metrics showing (b) the comparison between estimated force and true force and (c) the confusion matrix for texture recognition.

texture based on the vibration signal generated when the artificial skin slips across a surface. The architecture of the MIMO-CNN is shown in Fig. 8(a). It consists of three input channels, each handling one FBG signal, and two outputs for force estimation and texture classification, respectively. Before preprocessing, the acquired time series from all four sliding experiments (Table I) were down-sampled to 100 Hz to reduce computation load. After down sampling, the time series consists of 918589 data points which were then segmented into 300 ms intervals using a sliding window method with window length and stride length of 30 and stride length of 30. The contact and shear force values within the window are averaged across that window and then associated to the force outputs of that particular window. The resulting window-sampled output are formatted in the form of 30×3 wavelength values (per window) as the input, and 3 force values as well as

1 fabric class as the output. After window sampling, 30606 segments were generated. As the window length generally dictates the recognition time, a time window of 300 ms (30 × 10 ms) was selected such that the recognition time of the sensing system is around 300 ms, comparable to typical human recognition time towards different textures of around 400 ms [39]. These segmented time series were fed into convolutional layers where features were identified and extracted. The feature maps produced by the convolutional layer were passed through max-pooling layer, which effectively reduces spatial dimensions while preserving essential information. This process of convolution and max-pooling were repeated twice, forming a two-layer hierarchal feature extraction approach. The initial convolutional layer extracts low-level, simple features from the input FBG signals, while the subsequent convolutional layer builds upon these to extract higher-level, more complex feature representations. The features were then flattened into a 1D vector and fed into two parallel neural network branches: one for force estimation and the other for texture classification. The shared convolution layers allow the network to learn common features relevant to both tasks, while the separate neural network branches allow for independent optimization of model parameters for each task. This modularity is particularly advantageous for real-world applications where task requirements may evolve independently over time.

Fig. 8(b) shows the output metrices of the MIMO-CNN for force estimation and texture classification for 918589 test samples, where the estimated force vectors are plotted against the actual force values. The MIMO-CNN model achieved an R-squared value of 0.9618 with mean absolute error (MAE) of 0.025 N, 0.023 N, 0.036 N for X-direction shear, Y-direction shear and normal force, respectively. Fig. 8(c) depicts the confusion matrix of the MIMO-CNN estimation branch across 20 different textures at various sliding speeds and normal forces, achieving a classification accuracy of 94.06%. The high classification accuracy and strong correlation between estimated and actual force values demonstrate the MIMO-CNN's effectiveness in identifying features within multi-channel FBG responses and providing accurate force and texture estimations.

VI. Discussion

Generally, the presented artificial skin demonstrates robust capability for detecting multidirectional forces and identifying surface texture via vibrations. To build a comprehensive tactile perception system for robots, future work shall focus on integration of surface texture discrimination with material recognition capabilities via heat generation and perception [40]. Implementation of heat perception is also critical for temperature compensation, allowing the sensing system to compensate for thermal drifts. Although current work utilizes commercial table top interrogation system which is less practical for actual robotic integration, a miniaturized, low-power optical interrogator is currently under development and would be critical for robotic integration. The inherent multiplexing capability of FBGs also allows for seamless functional expansion on the artificial skin to cover larger areas of a robot and simultaneously measure other parameters such as skin stretch, finger joint angles and contact area, potentially realizing a multimodal, whole-body robotic sensing system with comprehensive recognition capability.

VII. Conclusion

This study introduces a tactile-sensitive artificial skin designed for robotic tactile applications. The artificial skin comprised of three FBG elements inscribed along a ZEONEX POF embedded within a silicon membrane. The use of POFs as the transmission medium allows tight bends and high-resolution tactile sensing across small areas without breakage, thanks to their low Young's modulus. The multiplexing capability of FBGs offers the opportunity for potential for large area tactile sensing with minimal fiber paths, and the skin-like form factor facilitates easy application on robotic surfaces without interference with other structures. The tactile-sensitive artificial skin was demonstrated on a fingertip model with dimensions similar to a human index finger, and its static force and slip-induced vibration characteristics were characterized. The collected force and vibrational responses were used to train a MIMO-CNN model, enabling simultaneous multidirectional force sensing and texture recognition. The data-driven nature of the MIMO-CNN model compensates for fabrication and placement errors, reducing the impact of fabrication tolerances. The MIMO-CNN achieved an R-squared score of 0.9618 for force estimation with tested normal force up to 10 N and shear forces around ±4 N in both the X and Y directions, as well as texture recognition accuracy of 94.06% for 20 tested textures. This robust combination of CNN and FBG array allows excellent scalability for both large and small and large-area tactile sensing applications on various robotic surfaces, with the potential expandability for other tactile stimuli and senses for enhanced object recognition.

References

[1] S. Sundaram, P. Kellnhofer, Y. Li, J. Y. Zhu, A. Torralba, and W. Matusik, "Learning the signatures of the human grasp using a scalable tactile glove," *Nature*, vol. 569, no. 7758, pp. 698–702, 2019, doi: 10.1038/s41586-019-1234-z.

[2] H. Xia *et al.*, "Shaping high-performance wearable robots for human motor and sensory reconstruction and enhancement," *Nat. Commun.*, vol. 15, no. 1, 2024, doi: 10.1038/s41467-024-46249-0.

[3] S. Mintchev, M. Salerno, A. Cherpillod, S. Scaduto, and J. Paik, "A portable three-degrees-of-freedom force feedback origami robot for human–robot interactions," *Nat. Mach. Intell.*, vol. 1, no. 12, pp. 584–593, 2019, doi: 10.1038/s42256-019-0125-1.

[4] N. Bai *et al.*, "A robotic sensory system with high spatiotemporal resolution for texture recognition," *Nat. Commun.*, vol. 14, no. 1, 2023, doi: 10.1038/s41467-023-42722-4.

[5] Z. Sun, M. Zhu, X. Shan, and C. Lee, "Augmented tactile-perception and haptic-feedback rings as human-machine interfaces aiming for immersive interactions," *Nat. Commun.*, vol. 13, no. 1, pp. 1–13, 2022, doi: 10.1038/s41467-022-32745-8.

[6] K. Yao *et al.*, "Encoding of tactile information in hand via skin-integrated wireless haptic interface," *Nat. Mach. Intell.*, vol. 4, no. 10, pp. 893–903, 2022, doi: 10.1038/s42256-022-00543-y.

[7] R. S. Dahiya, G. Metta, M. Valle, and G. Sandini, "Tactile sensing—From Humans to Humanoids," *IEEE Trans. Robot.*, vol. 26, no. 1, pp. 38-1-38–17, 2010, doi: 10.1201/b15474.

[8] R. S. Johansson and J. R. Flanagan, "Coding and use of tactile signals from the fingertips in object manipulation tasks," *Nat. Rev. Neurosci.*, vol. 10, no. 5, pp. 345–359, 2009, doi: 10.1038/nrn2621.

[9] R. S. Johansson and G. Westling, "Roles of glabrous skin receptors and sensorimotor memory in automatic control of precision grip

when lifting rougher or more slippery objects," *Exp. Brain Res.*, vol. 56, no. 3, pp. 550–564, 1984, doi: 10.1007/BF00237997.
[10] H. Yokoyama *et al.*, "Active touch sensing by multi-axial force measurement using high-resolution tactile sensor with microcantilevers," *IEEJ Trans. Sensors Micromachines*, vol. 134, no. 3, pp. 58–63, 2014, doi: 10.1541/ieejsmas.134.58.
[11] K. Kim, J. Ahn, Y. Jeong, J. Choi, O. Gul, and I. Park, "All-soft multiaxial force sensor based on liquid metal for electronic skin," *Micro Nano Syst. Lett.*, vol. 9, no. 1, 2021, doi: 10.1186/s40486-020-00126-9.
[12] X. Duan, S. Taurand, and M. Soleimani, "Artificial skin through super-sensing method and electrical impedance data from conductive fabric with aid of deep learning," *Sci. Rep.*, vol. 9, no. 1, pp. 1–11, 2019, doi: 10.1038/s41598-019-45484-6.
[13] W. Lin, B. Wang, G. Peng, Y. Shan, H. Hu, and Z. Yang, "Skin-Inspired Piezoelectric Tactile Sensor Array with Crosstalk-Free Row+Column Electrodes for Spatiotemporally Distinguishing Diverse Stimuli," *Adv. Sci.*, vol. 8, no. 3, pp. 1–11, 2021, doi: 10.1002/advs.202002817.
[14] J. Ham *et al.*, "Porous Dielectric Elastomer Based Flexible Multiaxial Tactile Sensor for Dexterous Robotic or Prosthetic Hands," *Adv. Mater. Technol.*, vol. 8, no. 3, pp. 1–10, 2023, doi: 10.1002/admt.202200903.
[15] H. Yu *et al.*, "Skin-Inspired Capacitive Flexible Tactile Sensor with an Asymmetric Structure for Detecting Directional Shear Forces," *Adv. Sci.*, vol. 11, no. 6, pp. 1–10, 2024, doi: 10.1002/advs.202305883.
[16] K. Morton, R. Ishizaki, Z. Chen, M. S. Sarwar, and J. D. W. Madden, "Soft Three-Axis Capacitive Force Sensor for Robotic E-Skin on Curved Surfaces," *IEEE Sensors Lett.*, vol. 7, no. 10, pp. 1–4, 2023, doi: 10.1109/LSENS.2023.3303082.
[17] J. H. Pu *et al.*, "Human Skin-Inspired Electronic Sensor Skin with Electromagnetic Interference Shielding for the Sensation and Protection of Wearable Electronics," *ACS Appl. Mater. Interfaces*, vol. 10, no. 47, pp. 40880–40889, 2018, doi: 10.1021/acsami.8b15809.
[18] L. Massari *et al.*, "Functional mimicry of Ruffini receptors with fibre Bragg gratings and deep neural networks enables a bio-inspired large-area tactile-sensitive skin," *Nat. Mach. Intell.*, vol. 4, no. 5, pp. 425–435, 2022, doi: 10.1038/s42256-022-00487-3.
[19] F. Durini *et al.*, "Soft large area FBG tactile sensors for exteroception and proprioception in a collaborative robotic manipulator," *2021 Smart Syst. Integr. SSI 2021*, pp. 2021–2024, 2021, doi: 10.1109/SSI52265.2021.9466957.
[20] C. Y. Leong, X. Cheng, J. Cui, D. S. Gunawardena, and H. Y. Tam, "Artificial Skin Based on Polymer Optical Fiber Bragg Grating Arrays for Robotic Tactile Perception," *J. Light. Technol.*, vol. 42, no. 8, pp. 3022–3029, 2024, doi: 10.1109/JLT.2023.3343833.
[21] D. J. Webb, "Fibre Bragg grating sensors in polymer optical fibres," *Meas. Sci. Technol.*, vol. 26, no. 9, 2015, doi: 10.1088/0957-0233/26/9/092004.
[22] X. Cheng, D. S. Gunawardena, C.-F. J. Pun, J. Bonefacino, and H.-Y. Tam, "Single nanosecond-pulse production of polymeric fiber Bragg gratings for biomedical applications," *Opt. Express*, vol. 28, no. 22, p. 33573, 2020, doi: 10.1364/oe.408744.
[23] J. Bonefacino, X. Cheng, C.-F. J. Pun, S. T. Boles, and H.-Y. Tam, "Impact of high UV fluences on the mechanical and sensing properties of polymer optical fibers for high strain measurements," *Opt. Express*, vol. 28, no. 2, p. 1158, 2020, doi: 10.1364/oe.378634.
[24] J. Bonefacino *et al.*, "Ultra-fast polymer optical fibre Bragg grating inscription for medical devices," *Light Sci. Appl.*, vol. 7, no. 3, p. 17161, 2018, doi: 10.1038/lsa.2017.161.
[25] J. Cui *et al.*, "Large-range torsion sensor based on twin-core polymeric optical fiber," *Opt. Laser Technol.*, vol. 174, no. November 2023, p. 110548, 2024, doi: 10.1016/j.optlastec.2024.110548.
[26] A. Chanda and G. Singh, *Mechanical Properties of Human Tissues*. Singapore, 2023. doi: 10.1007/978-981-99-2225-3_4.
[27] P. Humbert, F. Ferial, P. Agache, and H. I. Maibach, *Agache ' s Measuring the Skin*. 2017.
[28] N. Pittar, T. Winter, L. Falland-Cheung, D. Tong, and J. N. Waddell, "Scalp simulation – A novel approach to site-specific biomechanical modeling of the skin," *J. Mech. Behav. Biomed. Mater.*, vol. 77, no. June 2017, pp. 308–313, 2018, doi: 10.1016/j.jmbbm.2017.09.024.
[29] X. Feng, L. Guo-Yang, A. Ramier, A. M. Eltony, and Y. Seok-Hyun, "In vivo stiffness measurement of epidermis, dermis, and hypodermis using broadband Rayleigh-wave optical coherence elastography," *Acta Biomater*, vol. 146, pp. 295–305, 2022, doi: 10.1016/j.actbio.2022.04.030.In.
[30] D. S. Gunawardena *et al.*, "Regenerated polymer optical fiber Bragg gratings with thermal treatment for high temperature measurements," *Photonics Res.*, vol. 10, no. 4, p. 1011, 2022, doi: 10.1364/prj.453683.
[31] G. Corniani, Z. Lee, M. J. Carré, R. Lewis, B. P. Delhaye, and H. P. Saal, "Sub-surface deformation of individual fingerprint ridges during dynamic contact," pp. 1–12, 2023.
[32] J. James, "Multi-Finger Haptics: Analysis of Human Hand Grasp towards a Tripod Three-Finger Haptic Grasp model," *Sensors*, vol. 2022, 2022.
[33] R. S. Figliola and D. E. Beasley, "Theory and design for mechanical measurements," *Meas. Sci. Technol.*, vol. 7, no. 7, 1996, doi: 10.1088/0957-0233/7/7/016.
[34] C. Liang *et al.*, "Wide Range Strain Distributions on the Electrode for Highly Sensitive Flexible Tactile Sensor with Low Hysteresis," *ACS Appl. Mater. Interfaces*, vol. 15, no. 12, pp. 15096–15107, 2023, doi: 10.1021/acsami.2c21241.
[35] S. Komurasaki, H. Kajimoto, and H. Ishizuka, "Fundamental perceptual characterization of an integrated tactile display with electrovibration and electrical stimuli," *Micromachines*, vol. 10, no. 5, 2019, doi: 10.3390/mi10050301.
[36] S. Chun, W. Son, H. Kim, S. K. Lim, C. Pang, and C. Choi, "Self-Powered Pressure- and Vibration-Sensitive Tactile Sensors for Learning Technique-Based Neural Finger Skin," *Nano Lett.*, vol. 19, no. 5, pp. 3305–3312, 2019, doi: 10.1021/acs.nanolett.9b00922.
[37] K. Fukushima, "Neocognitron: A self-organizing neural network model for a mechanism of pattern recognition unaffected by shift in position," *Biol. Cybern.*, vol. 36, no. 4, pp. 193–202, 1980, doi: 10.1007/BF00344251.
[38] Y. LeCun, L. Bottou, Y. Bengio, and P. Haffner, "Gradient-based learning applied to document recognition," *Proc. IEEE*, vol. 86, no. 11, pp. 2278–2323, 1998, doi: 10.1109/5.726791.
[39] T. Kim, W. Bair, and A. Pasupathy, "Perceptual Texture Dimensions Modulate Neuronal Response Dynamics in Visual Cortical Area V4," *J. Neurosci.*, vol. 42, no. 4, pp. 631–642, 2022, doi: 10.1523/JNEUROSCI.0971-21.2021.
[40] C. Y. Leong, J. Cui, X. Cheng, and H.-Y. Tam, "Artificial skin using photothermal optical fibers for material identification," in *29th International Conference on Optical Fiber Sensors*, 2025, p. 410. doi: 10.1117/12.3062711.

Chern Yang Leong received his B.E. (Hons.) Electronics majoring in Nanotechnology from Faculty of Engineering, Multimedia University Malaysia in 2019. He is currently a Ph.D. student in Department of Electrical and Electronic Engineering, The Hong Kong Polytechnic University, Hong Kong SAR. His research interests include fiber Bragg grating sensors, thin-film electronics, polymer electronics and related fields for biomedical applications.

Jingxian Cui received the B.Sc. degree in optical engineering from University of Electronic Science and Technology of China, Chengdu, China, in 2015, and the M.Sc. degree in optical engineering from Huazhong University of Science and Technology, Wuhan, China, in 2018. She received the Ph.D. degree from the Department of Electrical Engineering, The Hong Kong Polytechnic University, Hong Kong SAR, in 2021, where she is currently a Postdoctoral Fellow. Her research interests include the design and fabrication of polymer optical fibers and fiber Bragg gratings for biomedical applications.

Xin Cheng received his M.S. and Ph.D. degrees from the Northeast Normal University and Jinan University in 2009 and 2019, respectively. In 2009, he joined the Photonic Research

Center of Hong Kong Polytechnic University (PolyU PRC) as Research Assistant and from 2019, where he was a Postdoctoral Fellow and now works as a Scientific Officer.

Lin Htein received his M.S. degree in Physics at Mandalay University, Myanmar, in 2005, and obtained his Ph.D. degree in Photonics and Applied Physics from Gwangju Institute of Science and Technology, South Korea, in 2014. Presently, he serves as a Research Associate at the Photonics Research Institute, Department of Electrical and Electronic Engineering in The Hong Kong Polytechnic University, Hong Kong SAR. His research focuses on the design and fabrication of specialty optical fibers for a wide range of sensing applications and the development of optical fiber devices.

Hwa-Yaw Tam (*Life Fellow*, *IEEE, Fellow, Optica*) received the B.Sc. and Ph.D. degrees in electrical and electronic engineering from The University of Manchester, Manchester, U.K., in 1985 and 1990, respectively. From 1989 to 1993, he was with the Hirst Research Centre, GEC-Marconi Ltd., London, U.K., working on optical components, WDM systems, and erbium optical fiber amplifiers. He is currently a Chair Professor of Photonics and the Associate Director of the Photonic Research Institute, The Hong Kong Polytechnic University, Hong Kong SAR. He is also the Director of the Southern Marine Science and Engineering Guangdong Laboratory, Zhuhai, China. He has developed optical fiber sensors and sensing networks for condition monitoring applications in Hong Kong SAR, Mainland China, Taiwan, Singapore, The Netherlands, Australia, and India. He has authored about 900 technical articles, has an H-index of 73 in Google Scholar, and holds 14 patents. His research interests include design and fabrication of specialty optical fibers for sensor applications and optical monitoring systems for railways, smart buildings, batteries, and medical devices.